ADVANCED ENERGY MATERIALS
www.advenergymat.de

Light Absorption and Recycling in Hybrid Metal Halide Perovskite Photovoltaic Devices

*Jay B. Patel, Adam D. Wright, Kilian B. Lohmann, Kun Peng, Chelsea Q. Xia, James M. Ball, Nakita K. Noel, Timothy W. Crothers, Jenny Wong-Leung, Henry J. Snaith, Laura M. Herz, and Michael B. Johnston**

The production of highly efficient single- and multijunction metal halide perovskite (MHP) solar cells requires careful optimization of the optical and electrical properties of these devices. Here, precise control of $CH_3NH_3PbI_3$ perovskite layers is demonstrated in solar cell devices through the use of dual source coevaporation. Light absorption and device performance are tracked for incorporated MHP films ranging from ≈67 nm to ≈1.4 µm thickness and transfer-matrix optical modeling is utilized to quantify optical losses that arise from interference effects. Based on these results, a device with 19.2% steady-state power conversion efficiency is achieved through incorporation of a perovskite film with near-optimum predicted thickness (≈709 nm). Significantly, a clear signature of photon reabsorption is observed in perovskite films that have the same thickness (≈709 nm) as in the optimized device. Despite the positive effect of photon recycling associated with photon reabsorption, devices with thicker (>750 nm) MHP layers exhibit poor performance owing to competing nonradiative charge recombination in a "dead-volume" of MHP. Overall, these findings demonstrate the need for fine control over MHP thickness to achieve the highest efficiency cells, and accurate consideration of photon reabsorption, optical interference, and charge transport properties.

1. Introduction

Metal halide perovskites have shown immense potential as light harvesting materials for thin film photovoltaic (PV) devices.[1,2] Single-junction PV devices incorporating perovskite thin films have now reached power conversion efficiencies (PCEs) of 25.2%, higher than any other thin film based PV technology such as those based on copper indium gallium selenide (CIGS) and CdTe.[3] The main advantage of metal halide perovskites over other thin film PV technologies is that they can be fabricated using various low temperature methods,[4–6] yielding films with benign defect chemistry, and optoelectronic properties ideal for efficient light harvesting.[7,8]

The perovskite crystal structure has the general chemical formula ABX_3, where A is a cation, B is a metal cation, and X is an anion. While the prototypical halide perovskite material is $CH_3NH_3PbI_3$, in the most commonly used perovskite compositions, a mixture of iodide and bromide are used at the X-site to tune the bandgap of the material. Further bandgap tuning and additional chemical and thermal stability can also be imparted through the incorporation of multiple cations at the A-site.[9–12] Perovskite thin films, with a range of compositions, can be fabricated via solution processes, vapor based processes, or a mixture of both, using readily available and inexpensive precursors.[9,13,14] The ability to fabricate and tune the bandgap of perovskite thin films in a variety of ways, provides an effective route to exceeding the Shockley–Queisser limit by creating cheap and highly efficient tandem and multijunction PV devices.

Multijunction PV devices can either be in a two- or four-terminal configuration.[15] A two-terminal multijunction configuration is ideal for thin film based solar cells, as they require fewer semi-transparent electrodes and thus have minimal optical losses.[15] Furthermore, two-terminal multijunction devices require the same number of costly auxiliary components, such as inverters, as single junction device, whereas four-terminal device configuration require at least twice as many.[16] Currently, the most efficient perovskite-based, two-terminal tandem device architecture incorporates a silicon bottom cell with a wide bandgap perovskite top cell.[3,17] While depositing perovskite thin films onto existing mass-produced silicon PV is likely to be the quickest way to the market in the short term, multijunction all-perovskite PV devices offer the possibility of higher efficiency and lower manufacturing costs in the long

Dr. J. B. Patel, Dr. A. D. Wright, K. B. Lohmann, Dr. K. Peng, C. Q. Xia, Dr. J. M. Ball, Dr. N. K. Noel, Dr. T. W. Crothers, Prof. H. J. Snaith, Prof. L. M. Herz, Prof. M. B. Johnston
Department of Physics
University of Oxford
Clarendon Laboratory
Parks Road, Oxford OX1 3PU, UK
E-mail: michael.johnston@physics.ox.ac.uk
Dr. N. K. Noel
Princeton Institute for the Science and Technology of Materials
Princeton University
Princeton, NJ 08540, USA
Prof. J. Wong-Leung
Research School of Physics
The Australian National University
Canberra, ACT 2601, Australia
The ORCID identification number(s) for the author(s) of this article can be found under https://doi.org/10.1002/aenm.201903653.

DOI: 10.1002/aenm.201903653

term if a number of practical hurdles can be overcome.[18,19] All-perovskite tandem PV devices also have additional advantages. For example, they are very thin and can be deposited on flexible substrates, making them suitable for use in scenarios where both the cost and power-to-weight ratio is important.[20]

Both silicon-perovskite and all-perovskite multijunction devices require intricate device architectures, where each layer needs special considerations to ensure that the device achieves maximum efficiency.[21–30] The current-voltage characteristics of individual sub-cells, light management throughout the device, and the chemical stability of the individual materials are the most important considerations when fabricating multijunction tandem PV devices.[9,28–31] In a two-terminal device configuration, the current (I) of the two subcells must match to ensure that there is a balance of electron and holes in the recombination layer.[32] Careful attention needs to be given to the light management of each layer to ensure that there are minimal reflection and scattering losses, and that maximum light is absorbed.[33] Currently, two-terminal multijunction all-perovskite tandem devices consist of 12 layers, each with different refractive indices.[16] As light propagates through the device, layers that absorb or reflect light from the AM 1.5 filtered solar spectrum contribute to an optical electric field profile due to phase coherence.[34] Therefore, fine tunability of the perovskite film thickness is important to maximize light absorption in the perovskite layer and ensure photocurrent is collected, hence maximizing the PCE of multijunction devices.[19]

While solution-based fabrication methods have produced the most efficient perovskite PV devices,[5] the techniques used are not readily scalable.[4,35] There are a number of challenges in upscaling solution-based perovskite fabrication methods. One challenge is that the solvents currently used in precursor solutions (such as dimethylformamide) are toxic and hence, expensive to use in an industrial setting.[36] Additionally, solvent usage poses a particular problem for multi-layer devices in that it is necessary to use solvents which can dissolve the perovskite precursors without partially or completely dissolving the proceeding layers. The thickness of solution processed films is also limited by the saturation concentration of the perovskite solution and it is challenging to obtain pin-hole-free films over a large area based on conventional solution deposition methods.[4,35]

In contrast, physical vapor deposition (PVD) is a dry process,[6] which produces uniform perovskite films and does not require solvents. As PVD is a solvent-free technique, it increases the range of substrates on which the perovskite can be deposited, and there is no upper limit to the range in thicknesses which can be deposited.[37] PVD, specifically thermal evaporation, has proven to be an effective fabrication technique to produce high quality planar heterojunction devices.[38] PVD can be used to fabricate perovskite films in two distinct ways, coevaporation and sequential evaporation/deposition.[39–42]

While sequentially evaporating the perovskite precursors has yielded films of respectable quality, it has disadvantages, the main being the requirement of an annealing step for thorough mixing of the precursors. Alternatively, coevaporation does not require any annealing step, expanding the number of substrates upon which the film can be deposited, as well as allowing finer control over the thickness of the film.[37,38,43] One disadvantage of coevaporation over the sequential deposition method is that controlling and optimizing the deposition rate of each precursor simultaneously is not trivial.[44] However, once the deposition rate of each precursor is optimized, the resultant films consist of a high-quality perovskite.[45] Organic transport layers have been shown to be the ideal surface for the vapor deposition of perovskite thin films[40] and have resulted in single-junction devices with 20.3% PCE.[38] Additionally, sequential deposition can be used in conjunction with solution processing, whereby one precursor layer is evaporated (typically the metal halide), with the other precursor layer (usually the precursor containing the organic cation) subsequently being deposited via spin/dip-coating.[14,46] While this combination of dry and wet techniques shows some promise,[31] extended annealing times are required to evaporate residual solvents, and there is little control over film thickness, rendering this process inadequate for upscaling of perovskite tandem devices.[14] Therefore, considering all requirements, coevaporation appears to be the ideal fabrication method for the deposition of both small and large-scale perovskite thin films, particularly those which are to be incorporated into two-terminal multijunction PV devices.

In this study, we investigate the optical effects that arise within PV devices as a result of varying the thickness of the perovskite layer. Single junction PV devices were fabricated incorporating perovskite thin films ranging from ≈67 nm to ≈1.4 µm. Fourier transform photocurrent and absorption spectroscopy were combined with optical simulations to explain the variation of device performance with thickness. Overall, the results show that the optimal perovskite ($CH_3NH_3PbI_3$) thin film thickness is ≈700 nm in a single junction PV device, and that subsequent increases in film thickness lead to a reduction in both the J_{sc} and V_{oc} and consequently, the PCE.

2. Results and Discussion

The perovskite thin films were fabricated by coevaporation of CH_3NH_3I and PbI_2 under high vacuum (≈10^{-6} mbar) for various time intervals. Full experimental details and the determination of the evaporation rate can be found in the Supporting Information. **Figure 1**a shows a photograph of PV devices with a wide range (≈67 nm to ≈1.4 µm) of perovskite thicknesses. The thicknesses were measured using scanning electron microscopy (SEM) images shown in Figure 1b. From the photograph, it is evident that as the perovskite thickness is increased, the devices change from being semi-transparent to completely opaque. The cross-sectional SEM images (Figure 1b) of the devices shown in Figure 1a clearly show the increase in perovskite thickness. Additional cross-sectional images of the devices can be found in the Supporting Information (Figure S1). The devices were fabricated on fluorine doped tin oxide (FTO) coated glass substrates, and consisted of an evaporated C_{60} electron transport layer (≈10 nm thick as determined by elemental line scan analysis shown in Figure S2, Supporting Information), a $CH_3NH_3PbI_3$ perovskite layer of specified thickness (Figure 1), a ≈250 nm thick 2,2′,7,7′-tetrakis[*N*,*N*-di(4-methoxyphenyl)-amine]-9,9′-spirobifluorene (Spiro-OMeTAD) hole transport layer and a ≈100 nm gold electrode. Interestingly, the cross-sectional images show that as the perovskite film becomes thicker (≥ ≈709 nm), the cross-section incorporates fewer grains that stack upon each

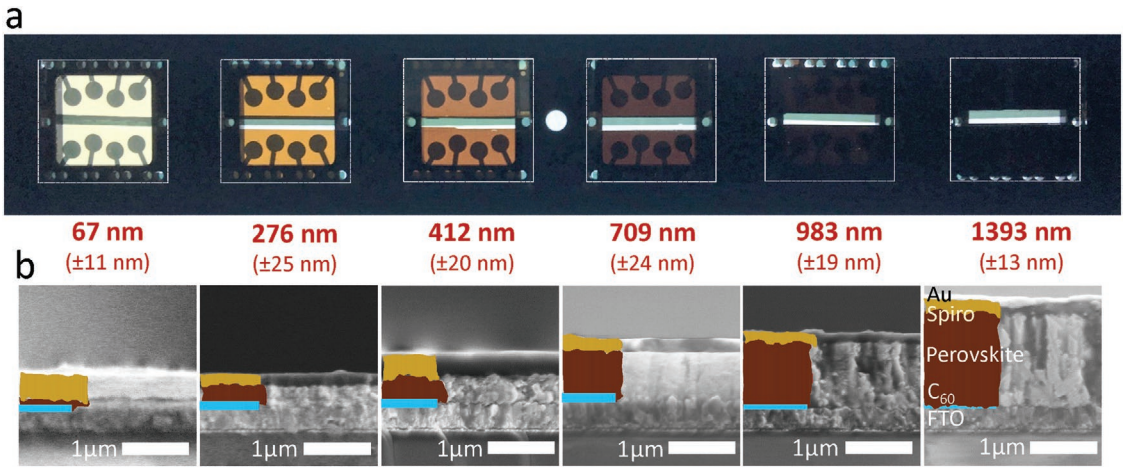

Figure 1. a) Photographs of the perovskite PV devices encompassing different thickness of perovskite ($CH_3NH_3PbI_3$) thin films. Images are of the front of the devices (glass side), showing light transmitted through the solar cells, which were back-illuminated. Each substrate encompasses eight circular pixels with an active area of 0.0919 cm^2. b) Cross-sectional SEM images of $CH_3NH_3PbI_3$ devices with differing perovskite absorber thickness, the scale bar represents 1 μm. The device structure (with corresponding shaded color) is FTO/C_{60}(blue)/ Perovskite, $CH_3NH_3PbI_3$(brown)/Spiro-OMeTAD(yellow)/Au. See the Supporting Information for further details of device fabrication and larger SEM images.

other, and instead tends toward large columnar like structures extending from the bottom to the top of the cross-section. This change in morphology was accompanied by changes in crystalline disorder. Figure S3 (Supporting Information) shows the Urbach energy (E_u), which provides an indicator of structural disorder,[47,48] as a function of perovskite layer thickness within the PV devices. E_u increased from 15 to 17.3 meV for devices with perovskite thin film thickness between ≈67 and ≈412 nm followed by a sharp decrease to 14 meV and down to 12.4 meV for thicker devices exhibiting the columnar morphology. Thus, it appears that the transition to a columnar morphology is also associated with a decrease in structural disorder and hence increased crystallinity. Previous results have shown that the grain sizes in coevaporated perovskite films to be relatively small compared to those in solution processed films.[6,39,40,49] The small grains will lead to an increase in the quantity of grain boundaries, which may result in an increase of trap states, and negatively impact the PCE. Therefore, the above SEM images show that modulating the thickness of perovskite films is a way of changing the morphology, which is a significant step towards morphological control in coevaporated perovskite films.

We now explore the process of light absorption and photocurrent collection by comparing the absorptance and external quantum efficiency (EQE) of the devices presented in Figure 1. Absorptance gives the probability of a photon of specific energy being absorbed in any part of the device structure, while EQE records the likelihood of a photon being absorbed in the active layer *and* producing electron-hole pairs that are extracted from the device. Therefore, comparing absorptance and EQE spectra is a powerful way of determining sources of efficiency loss in PV devices. **Figure 2**a displays the absorptance spectra of the planar heterojunction PV devices with differing perovskite film thicknesses. The total absorption of a device includes the parasitic absorption of transport materials and the electrode, as well as optical interference effects that arise within the device due to the different dielectric constants for each material.[33,34,50] From Figure 2a, it is evident that when the perovskite absorber layer is ≈67 nm the absorption is strongest for shorter wavelengths of light. Conversely, when the device encompasses a ≈1.4 μm perovskite film, most of the photons with energy equal to or greater energy than the bandgap are absorbed, as shown by the steep absorption onset at 780 nm in Figure 2a. The EQE spectra in Figure 2b show a similar trend to the absorption spectra in Figure 2a. As the absorption of longer wavelengths of light increases with increasing perovskite film thickness (Figure 2a), there is a corresponding increase in the EQE at longer wavelengths.[51] A key exception to the trend is that the overall magnitude of the external quantum efficiency (EQE) spectrum is much lower for the device incorporating ≈1.4 μm perovskite film than the EQE of devices encompassing ≈412 nm, ≈709 nm and ≈983 nm thick perovskite films. The reason for the reduction in quantum efficiency can be attributed to a drop in charge collection efficiency. As the perovskite absorber layer becomes thicker, it will absorb more light. However, the charge carriers generated at the surface (holes in this study, as we are investigating *n-i-p* device architecture) will have to travel farther to reach the charge extraction layer (Spiro-OMeTAD).[52–54]

In multilayer devices light absorption does not necessarily follow a simple Beer-Lambert profile as a result of interference effects originating from changes in the dielectric constant between all the different layers.[55] Such interference effects are particularly important in our PVD deposited devices owing to the high uniformity and smoothness of the coevaporated films. As such, these effects can be exploited to improve solar cell device efficiency through careful selection of each layer in a device. Oscillations can be clearly observed in the EQE spectra in Figure 2b for the ≈67 nm, ≈276 nm, ≈412 nm, and ≈709 nm thick films. Using dielectric constants for all layers of our device structure we used a transfer matrix approach to reproduce the measured device absorption spectra (detailed information of the modeling can be found in the Supporting Information).[33,54] Figure 2c shows the simulated absorption spectra for the devices shown in Figure 1 using the transfer matrix method described by Burkhard et al.[34] The simulated absorption spectra show

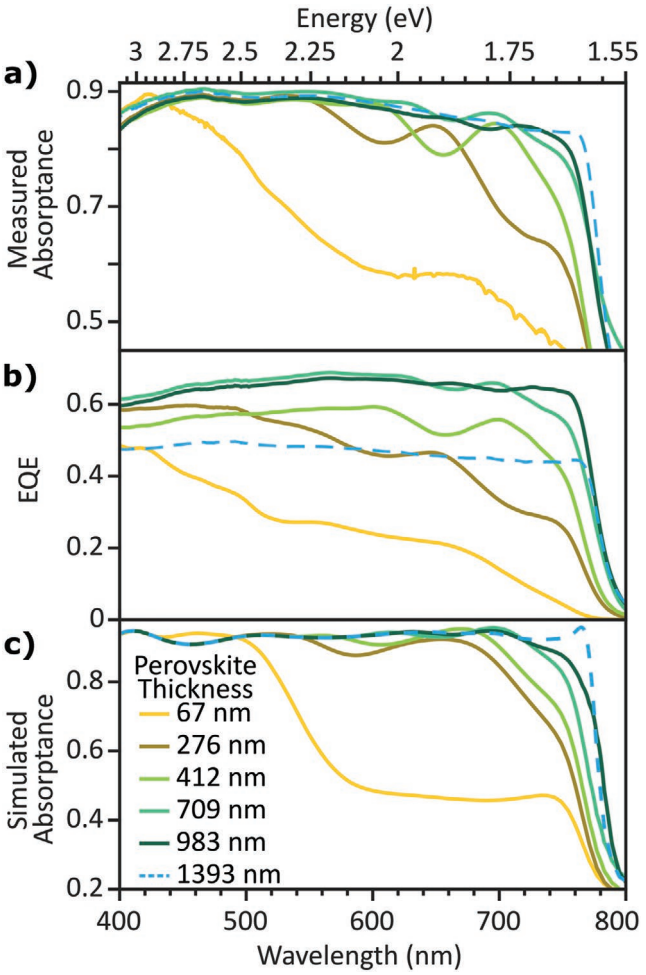

Figure 2. a) The measured absorption spectra of the devices shown in Figure 1. b) The external quantum efficiency (EQE) of the devices shown in Figure 1. c) The simulated absorption spectra for full devices (as shown in Figure 1) incorporating different thickness of perovskite thin films. The absorption spectra were simulated using a transfer matrix model created by Burkhard et al.[34] Detailed information of the model used can be found in the Supporting Information.

similar interference patterns as the measured absorption spectra. In multijunction devices, careful design of layers in the entire device is needed to maximize absorption of spectral bands in the perovskite regions of corresponding sub-cells, while maintaining current matching through all sub-cells.

To better understand how optical interference in absorption and EQE spectra impact photocurrent generation, we carried out further optical simulations. Maps of the optical electric field (|**E**|) within illuminated devices employing six different perovskite film thicknesses are displayed in **Figure 3**a. The maps were produced using a transfer matrix model[34] based on the device architectures shown in Figure 1 (details of the simulation and the dielectric functions used for each device stack layer are provided in the Supporting Information). The thinner perovskite layers transmit a significant amount of green and red light through to the Spiro-OMeTAD and gold electrode, which is then reflected back into the device. The reflection of green and red light from the gold, results in the device acting as an optical cavity and the formation of standing waves within the whole device. Figure 3b shows the generation rate within the perovskite thin films of different thickness in the device. The wave-like modulations in the generation rate are a result of the optical interference effects observable in Figure 3a. As the thickness of the film is increased, most light is absorbed on a single pass and hence optical interference affects the device less. Figure 3c shows the short-circuit current density as a function of perovskite thickness, extracted from the simulated 100% internal quantum efficiency spectra. As the perovskite thickness is increased from 67 to 709 nm the optical interference has a significant effect on photocurrent generation (Figure 3c). The current density curve then flattens and reaches a plateau after increasing the perovskite thin film thickness from 709 nm to 1.398 μm, as there is maximum light absorption and little optical interference in the perovskite layer (Figure 2c & 3a)iv)). When the perovskite film thickness is ≈709 nm (Figure 2a,b), the total number of photogenerated carriers reaches a plateau, thus any additional perovskite volume does not result in an increase in photogenerated carriers and is effectively considered "dead volume."[56] This dead volume will consist of recombination sites, leading to a reduction in J_{sc} as the carriers drift from the front surface of the device to the back. The addition of perovskite dead volume has an impact in the J_{sc} as shown in the device EQE spectrum for devices with ≈1.4 μm thick perovskite thin film (Figure 2b).

The consequence of optical interference in the device is twofold: there will be losses in photocurrent as certain wavelengths of light are not entirely absorbed, and any changes in the thickness of other layers in the device will result in a change in the optical interference pattern. Hence, the thickness of the perovskite film, in combination with the other dielectric layers, will have to be optimized to maximize absorption. The solution is to find a thickness of the perovskite layer which maximizes the fraction of light absorbed, without being so thick as to result in dead volume, thus reducing the charge collection efficiency of the device.

Optical and device modeling using a transfer matrix approach should, in theory, allow the design of optimized solar cells. However, metal halide perovskites are direct bandgap semiconductors with high photoluminescence (PL) quantum yields. If PL is emitted as a result of the recombination of photogenerated electrons and holes, then the PL can be lost from the solar cell or be reabsorbed. Thus, the picture presented in Figure 3 will be modified by PL emission and reabsorption.

To assess the importance of photon reabsorption (also called photon "recycling") in our $CH_3NH_3PbI_3$ perovskite films we investigated the PL emission spectrum as a function of layer thickness. **Figure 4** shows the PL spectra of three different thicknesses of coevaporated $CH_3NH_3PbI_3$ films on quartz substrates. Figure 4a shows the PL spectra of the thin films where the PL is collected from the excitation spot. While the ≈412 nm thick perovskite thin film shows a typical Gaussian-like PL spectrum,[45] the ≈709 nm film shows a pronounced shoulder at longer wavelengths and the ≈983 nm film shows a double peak. The increasing red-shifting of the PL emission with increasing layer thickness is consistent with reabsorption and hence filtering of the "true" PL spectrum. The photon reabsorption effect leads to a more heavily filtered PL spectrum with increasing distance from the original excitation volume.[54]

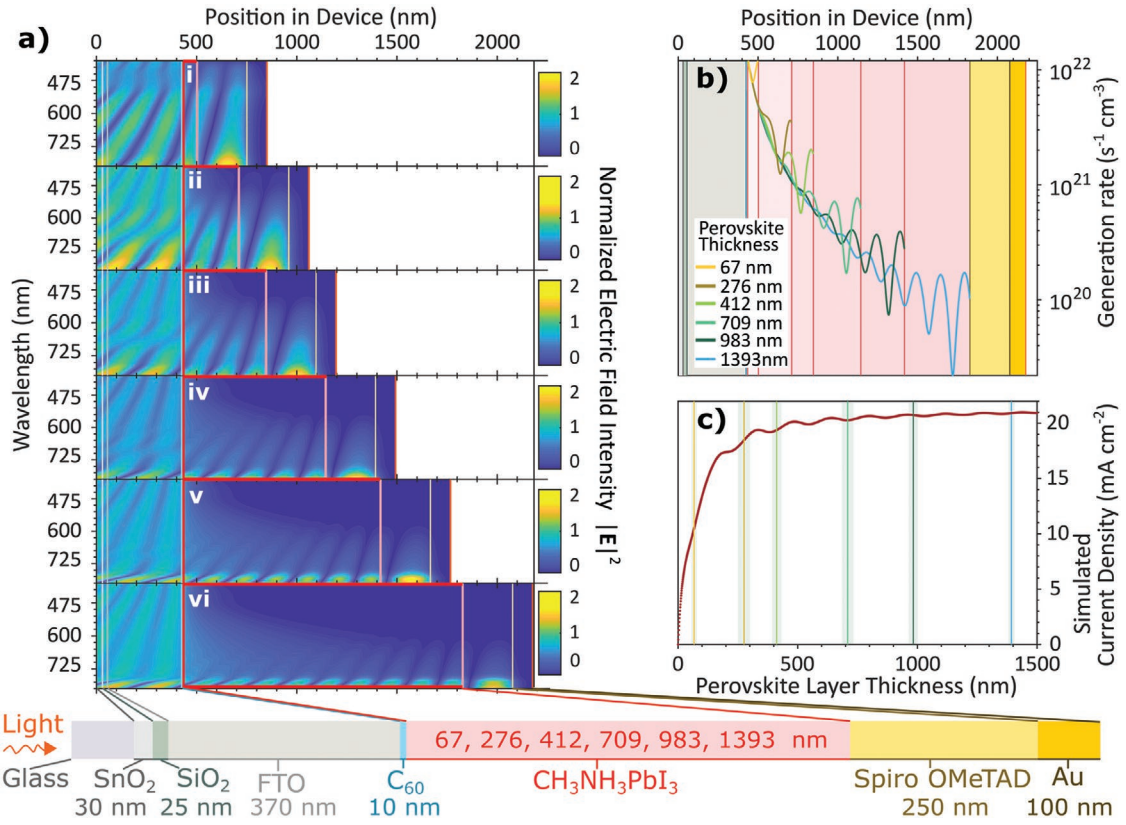

Figure 3. a) Simulation of the optical electric field within photovoltaic devices incorporating different thicknesses of perovskite thin films. The simulations show devices that incorporate i) 67 nm, ii) 276 nm, iii) 412 nm, iv) 709 nm, v) 983 nm, and vi) 1393 nm perovskite thin film thicknesses. The schematic at the bottom shows the direction of the incident light and the arrangement of layers and their thicknesses in the simulated device. b) The generation rate of different thicknesses of perovskite thin films at different positions in the device. c) The calculated current density as function of perovskite thin film thickness if there is 100% internal quantum efficiency. The lines show the perovskite thin film thicknesses investigated in this study, with shaded areas showing the error in the measured thickness.

Therefore, by measuring the PL spectrum at a spot laterally separated from the laser excitation spot it is possible to confirm the observation of photon reabsorption. Figure 4b,c shows PL collected from 1 mm on either side of a laser excitation spot (⌀ = 0.154 mm). The double PL peak observed in the ≈983 nm thick film has diminished, with only the lower energy peak being observable. This observation of only a lower energy peak in thick $CH_3NH_3PbI_3$ is confirmation that photon reabsorption is significant within the perovskite thin film and should be included when devices are optically modeled. The PL spectra of different thicknesses of perovskite, corrected for photon reabsorption, are shown in Figure 4d–f, obtained using the model described by Crothers et al.[54] (further details can be found in the Supporting Information). Accounting for reabsorption reveals that the PL spectra emitted within the films do not vary significantly between the different thicknesses of films for the three different detection locations as shown in Figure 4d–f.

Figure 5 shows the device characteristics of devices with 9 different perovskite thin film thicknesses ranging from ≈67 nm to ≈1.4 µm. The steady-state power output (SPO) at constant applied bias is a metric determined by holding the device under constant applied bias (close to the voltage at maximum power) for between 20 and 60 s and calculating the power conversion efficiency. The champion devices for each thickness in this study were determined as the device with highest SPO (shown as red diamonds in Figure 5). Device JV curves, statistics and statistical analysis of multiple batches can be found in the Supporting Information. The highest SPO, 19.2%, was attained in the device incorporating a ≈709 nm thick perovskite film. Figure 5 shows two regimes of device characteristics; Regime A (blue shaded region) highlights device characteristics of solar cells that incorporate perovskite thin films ≤709 nm and Regime B (green shaded region), shows device characteristics of solar cells that incorporate perovskite films of thicknesses ≥709 nm. Correlation coefficients (ρ) were calculated to elucidate the relationship between the thickness of the perovskite film and individual device characteristics such as PCE, SPO at constant applied bias, short-circuit current density (J_{sc}), steady-state current density (J_{spo}) at constant applied bias, open-circuit voltage (V_{oc}), and fill factor(FF).

As the perovskite film thickness is increased from ≈67 to ≈709 nm (regime A) there is a strong positive correlation with the PCE, which rises from 3.2% to 16.5%. The correlation between PCE and thickness in regime A is further reflected in the SPO, where the SPO increases from 3.4% to 19.2%. However, as the thickness is increased from ≈709 nm to ≈1.4 µm (regime B) there is a strong negative correlation with the PCE and SPO. The PCE is directly proportional to the J_{sc}, V_{oc}, and FF, therefore any

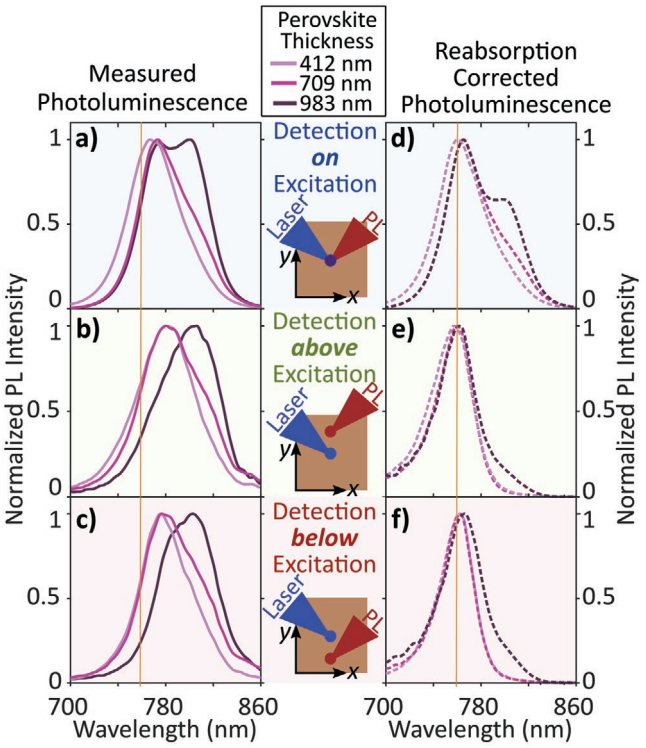

Figure 4. The measured time-integrated photoluminescence (PL) spectra of perovskite thin films (left column, solid lines), of three different perovskite thin film thicknesses (as shown by the legend) at a) directly on the excitation spot, b) 1 mm above the excitation spot, and c) 1 mm below the excitation spot. A 398 nm pulsed diode laser with a fluence of 300 nJ cm^{-2} was used to obtain the PL spectra. Photon reabsorption-corrected PL spectra (right column, dotted lines) d) directly on the excitation spot, e) 1 mm above the excitation spot, and f) 1 mm below the excitation spot. The vertical line indicates a wavelength of 760 nm.

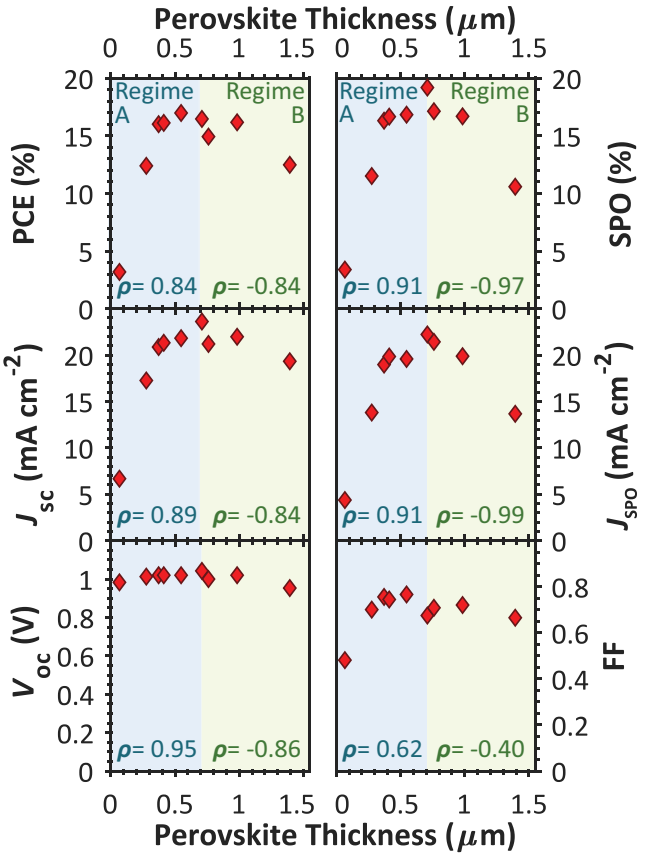

Figure 5. The device characteristics of vapor-deposited perovskite devices with different thicknesses of $CH_3NH_3PbI_3$. The plots show the power conversion efficiency (PCE), the steady-state power output (SPO) at constant applied bias, the short-circuit current density (J_{sc}), the steady-state current density (J_{spo}) at constant applied bias, the open-circuit voltage (V_{oc}), and the fill factor (FF). The red markers represent parameters obtained from *J–V* characterization of the devices with the highest SPO at each thickness. The blue shaded region signifies devices that incorporate perovskite thin films ≤709 nm and is termed as "Regime A." The green shaded region signifies devices that incorporate perovskite thin films ≥709 nm and is termed as "Regime B." The correlation coefficient (ρ) was obtained using MATLAB. The statistical analysis was carried out to ensure that trends observed were of statistical significance. Device statistics and the corresponding statistical analysis can be found in the Supporting Information.

strong trends observed between the thickness of the perovskite film and these metrics will also influence the PCE.

As expected, the J_{sc} has a strong positive correlation with increasing perovskite thickness (≈67 to ≈709 nm (regime A)). The high absorption coefficient, α, of $CH_3NH_3PbI_3$ (Figure S4, Supporting Information), means that any slight increase in its thickness will result in an increase in photogenerated carrier concentration. The J_{spo} also shows a strong positive correlation with thickness in regime A. In regime B, both the J_{sc} and J_{spo} show a strong negative correlation as the thickness of the perovskite film is increased from ≈709 nm to ≈1.4 µm. As the perovskite film approaches a critical thickness, the charge collection efficiency starts to decrease (as shown in Figure 2b),[52,53] which will result in a decrease in device J_{sc}. The J_{spo} shows a larger decrease that the J_{sc} in regime B. The larger drop is likely due to the charge carrier transport being governed by diffusion under forward bias near the maximum power point, whereas at J_{sc} the dominant transport mechanism is drift.[56]

In regime A, the V_{oc} shows a strong positive correlation with perovskite film thickness, which can be attributed to the increase in J_{sc} in the same regime. Moreover, thinner perovskite films have a larger surface area to volume ratio. Therefore, the lower V_{oc} of the device containing ≈67 nm thick perovskite film may also be due to the increased impact of surface recombination on the total recombination rate.[57] As the perovskite film thickness is further increased from ≈709 nm (regime B), the V_{oc} begins to drop. This is contrary to what we observe in the Urbach energy, where E_u decreases as the thickness of the perovskite thin film increase in the devices (Figure S3, Supporting Information). A decrease in E_u typically results in a higher V_{oc} as the density of tail states decreases.[58,59] The drop in V_{oc} in regime B is therefore most likely due the reduction in steady-state carrier density, as the thickness of absorber material increases, as explained by Brendal and Queisser.[60] From Figure 2a,b, we can see that a device incorporating a ≈709 nm perovskite film absorbs most of the incident light. However, as the thickness of the perovskite is increased to ≈1.4 µm, there is no significant increase in photogenerated charge carriers, yet the volume of perovskite is doubled. As the recombination lifetimes and mobility of evaporated metal halide perovskite

films are relatively low (Figure S8, Supporting Information), compared to solution processed perovskite films, the diffusion lengths are also smaller.[61] The lower diffusion length will result in a reduction of diffused charge carriers into the perovskite dead volume and toward the back-transport layer (Spiro-OMeTAD in this study). Therefore, due to the perovskite dead volume there will be a reduction in the electric field across the perovskite layer thus leading to a reduction in V_{oc}.[60,62–65]

The FF shows a weak positive correlation with film thickness in regime A, and a very weak negative correlation in regime B. These observations show that two of the factors which can influence the FF, series resistance and shunt resistance, are not affected by the increase in perovskite thin film thickness. Figure S9 (Supporting Information) shows the series and shunt resistance calculated using the *JV* curves of the champion devices. Both the series and shunt resistances show no correlation in region A, however, in region B the shunt resistance shows a negative correlation.

The trends observed in the device characteristics as a function of perovskite film thickness show that optimizing the thickness of the perovskite to maximize light absorption and prevent the formation of excess perovskite (dead volume) will result in devices with the highest PCEs. Moreover, even though different compositions of metal halide perovskite films will have slight variations in their optoelectronic properties, the importance of finding the correct thickness of the perovskite films will be critical for any composition to prevent "dead volumes" and to maximize light absorption in the thin film. Further gains in key device parameters can then be attained by incorporating charge transport layers that have better energetic band alignment with different interfaces, which will also help to maximize the PCE. For example, Figure S10 (Supporting Information) shows two different device architectures, both employing perovskite films (≈709 nm) which were deposited in the same evaporation run. The *J–V* curves of these devices show that incorporating a wide bandgap SnO_2 electron transport layer (n-type) into the device stack increases the V_{oc} as a result of better energetic band alignment between the perovskite/C_{60} and the FTO. On the other hand, the J_{sc} is identical for both the device architectures because the thickness of the photoabsorbing perovskite layer is the same for both devices. As the above results show, in a multilayer planar heterojunction PV device, each layer must have optimal energetic alignment and the correct photoabsorber thickness, to ensure that the maximum V_{oc} and J_{sc} are extracted. Therefore, optimal energetic alignment and effective light management becomes even more important in multijunction devices, where ensuring current matching between different cells while extracting the highest voltage for individual cells is critical to achieving highly efficient tandem devices.

3. Conclusion

In summary, through varying the thickness of the perovskite absorber layer in photovoltaic devices, this investigation has illustrated the importance of light management within the overall device architecture. A thinner than optimum perovskite film thickness will result in optical losses due to optical interference effects. As shown by modeling the light absorption in the devices, the multilayer devices were found to act as an optical cavity. Therefore, devices featuring thinner perovskite films will lead to the development of strong unfavorable optical interference patterns within the device and results in a reduction in the total absorbed light. A thicker than optimum perovskite film thickness will result in a perovskite "dead volume," which will reduce the overall device voltage and charge carrier collection efficiency as observed in the current-voltage characteristics and EQE spectra. Furthermore, as shown by the PL measurements, thicker perovskite thin films will be affected by photon reabsorption effects which need to be accounted for when determining the optimum thickness. Therefore, to achieve the highest efficiency photovoltaic devices, the optimum thickness of the perovskite film should absorb the maximum amount of light, contain minimal dead volume and be interfaced with transport materials that have ideal energetic band alignment. This investigation clearly shows that thermal coevaporation is the ideal tool for deposition of high quality and uniform perovskite films with precisely controlled thicknesses.

Supporting Information

Supporting Information is available from the Wiley Online Library or from the author.

Acknowledgements

The authors gratefully acknowledge financial support from the Engineering and Physical Science Research Council (UK) grant numbers EP/P006329/1, EP/P033229/1. M.B.J. thanks the Humboldt Foundation for support.

Conflict of Interest

H.J.S. is the co-founder and CSO of Oxford PV Ltd, a company that is commercializing perovskite photovoltaic technologies. The other authors declare no competing interests.

Keywords

light management, photon reabsorption, quantum efficiency, thickness dependence, vapor deposition

Received: November 6, 2019
Revised: December 11, 2019
Published online:

[1] M. M. Lee, J. Teuscher, T. Miyasaka, T. N. Murakami, H. J. Snaith, *Science* **2012**, *338*, 643.
[2] H.-S. Kim, C.-R. Lee, J.-H. Im, K.-B. Lee, T. Moehl, A. Marchioro, S.-J. Moon, R. Humphry-Baker, J.-H. Yum, J. E. Moser, M. Grätzel, N.-G. Park, *Sci. Rep.* **2012**, *2*, 591.
[3] NREL, Best Research-Cell Efficiency Chart. www.nrel.gov/pv/cell-efficiency.html (accessed: October 2019).
[4] Z. Li, T. R. Klein, D. H. Kim, M. Yang, J. J. Berry, M. F. A. M. van Hest, K. Zhu, *Nat. Rev. Mater.* **2018**, *3*, 18017.

[5] Q. Jiang, Y. Zhao, X. Zhang, X. Yang, Y. Chen, Z. Chu, Q. Ye, X. Li, Z. Yin, J. You, *Nat. Photonics* **2019**, *13*, 460.
[6] J. Ávila, C. Momblona, P. P. Boix, M. Sessolo, H. J. Bolink, *Joule* **2017**, *1*, 431.
[7] L. M. Herz, *Annu. Rev. Phys. Chem.* **2016**, *67*, 65.
[8] L. M. Herz, *ACS Energy Lett.* **2017**, *2*, 1539.
[9] N. J. Jeon, J. H. Noh, W. S. Yang, Y. C. Kim, S. Ryu, J. Seo, S. Il Seok, *Nature* **2015**, *517*, 476.
[10] G. E. Eperon, S. D. Stranks, C. Menelaou, M. B. Johnston, L. M. Herz, H. J. Snaith, *Energy Environ. Sci.* **2014**, *7*, 982.
[11] N. K. Noel, S. D. Stranks, A. Abate, C. Wehrenfennig, S. Guarnera, A.-A. Haghighirad, A. Sadhanala, G. E. Eperon, S. K. Pathak, M. B. Johnston, A. Petrozza, L. M. Herz, H. J. Snaith, *Energy Environ. Sci.* **2014**, *7*, 3061.
[12] D. P. McMeekin, G. Sadoughi, W. Rehman, G. E. Eperon, M. Saliba, M. T. Horantner, A. Haghighirad, N. Sakai, L. Korte, B. Rech, M. B. Johnston, L. M. Herz, H. J. Snaith, *Science* **2016**, *351*, 151.
[13] M. Liu, M. B. Johnston, H. J. Snaith, *Nature* **2013**, *501*, 395.
[14] J. Werner, C.-H. Weng, A. Walter, L. Fesquet, J. P. Seif, S. De Wolf, B. Niesen, C. Ballif, *J. Phys. Chem. Lett.* **2016**, *7*, 161.
[15] G. E. Eperon, M. T. Hörantner, H. J. Snaith, *Nat. Rev. Chem.* **2017**, *1*, 0095.
[16] R. Fu, D. Feldman, R. Margolis, *US Solar Photovoltaic System Cost Benchmark: Q1 2018*, National Renewable Energy Laboratory, Golden, Colorado **2018**.
[17] F. Sahli, J. Werner, B. A. Kamino, M. Bräuninger, R. Monnard, B. Paviet-Salomon, L. Barraud, L. Ding, J. J. Diaz Leon, D. Sacchetto, G. Cattaneo, M. Despeisse, M. Boccard, S. Nicolay, Q. Jeangros, B. Niesen, C. Ballif, *Nat. Mater.* **2018**, *17*, 820.
[18] G. E. Eperon, T. Leijtens, K. A. Bush, R. Prasanna, T. Green, J. T.-W. Wang, D. P. McMeekin, G. Volonakis, R. L. Milot, R. May, A. Palmstrom, D. J. Slotcavage, R. A. Belisle, J. B. Patel, E. S. Parrott, R. J. Sutton, W. Ma, F. Moghadam, B. Conings, A. Babayigit, H.-G. Boyen, S. Bent, F. Giustino, L. M. Herz, M. B. Johnston, M. D. McGehee, H. J. Snaith, *Science* **2016**, *354*, 861.
[19] M. T. Hörantner, T. Leijtens, M. E. Ziffer, G. E. Eperon, M. G. Christoforo, M. D. McGehee, H. J. Snaith, *ACS Energy Lett.* **2017**, *2*, 2506.
[20] A. F. Palmstrom, G. E. Eperon, T. Leijtens, R. Prasanna, S. N. Habisreutinger, W. Nemeth, E. A. Gaulding, S. P. Dunfield, M. Reese, S. Nanayakkara, T. Moot, J. Werner, J. Liu, B. To, S. T. Christensen, M. D. McGehee, M. F. A. M. van Hest, J. M. Luther, J. J. Berry, D. T. Moore, *Joule* **2019**.
[21] Q. Xu, Y. Zhao, X. Zhang, *Sol. RRL* **2019**, *3*, 1900206.
[22] Y. Chen, S. Tan, N. Zhou, N. Yang, W. Zhou, Y. Wu, K. Weber, Q. Chen, H. Zhou, *Sol. RRL* **2019**, *3*, 1900083.
[23] Y. Wu, A. Fell, K. J. Weber, *Sol. RRL* **2018**, *2*, 1800193.
[24] W. Ahmad, J. Khan, G. Niu, J. Tang, *Sol. RRL* **2017**, *1*, 1700048.
[25] Y. Zhang, Z. Wu, P. Li, L. K. Ono, Y. Qi, J. Zhou, H. Shen, C. Surya, Z. Zheng, *Adv. Energy Mater.* **2018**, *8*, 1701569.
[26] S. Zhu, F. Hou, W. Huang, X. Yao, B. Shi, Q. Ren, J. Chen, L. Yan, S. An, Z. Zhou, H. Ren, C. Wei, Q. Huang, Y. Li, G. Hou, X. Chen, Y. Ding, G. Wang, B. Li, Y. Zhao, X. Zhang, *Sol. RRL* **2018**, *2*, 1800176.
[27] S.-Y. Chang, Y.-C. Lin, P. Sun, Y.-T. Hsieh, L. Meng, S.-H. Bae, Y.-W. Su, W. Huang, C. Zhu, G. Li, K.-H. Wei, Y. Yang, *Sol. RRL* **2017**, *1*, 1700139.
[28] Y. Hu, L. Song, Y. Chen, W. Huang, *Sol. RRL* **2019**, *3*, 1900080.
[29] M. Jaysankar, M. Filipič, B. Zielinski, R. Schmager, W. Song, W. Qiu, U. W. Paetzold, T. Aernouts, M. Debucquoy, R. Gehlhaar, J. Poortmans, *Energy Environ. Sci.* **2018**, *11*, 1489.
[30] J. Hu, Q. Cheng, R. Fan, H. Zhou, *Sol. RRL* **2017**, *1*, 1700045.
[31] Z. Liu, L. Qiu, E. J. Juarez-Perez, Z. Hawash, T. Kim, Y. Jiang, Z. Wu, S. R. Raga, L. K. Ono, S. Liu, Y. Qi, *Nat. Commun.* **2018**, *9*, 3880.
[32] A. De Vos, *J. Phys. D: Appl. Phys.* **1980**, *13*, 839.
[33] J. M. Ball, S. D. Stranks, M. T. Hörantner, S. Hüttner, W. Zhang, E. J. W. Crossland, I. Ramirez, M. Riede, M. B. Johnston, R. H. Friend, H. J. Snaith, *Energy Environ. Sci.* **2015**, *8*, 602.
[34] G. F. Burkhard, E. T. Hoke, M. D. McGehee, *Adv. Mater.* **2010**, *22*, 3293.
[35] R. Swartwout, M. T. Hoerantner, V. Bulović, *Energy Environ. Mater.* **2019**, *2*, 119.
[36] C. J. Clarke, W.-C. Tu, O. Levers, A. Bröhl, J. P. Hallett, *Chem. Rev.* **2018**, *118*, 747.
[37] C. Momblona, O. Malinkiewicz, C. Roldán-Carmona, A. Soriano, L. Gil-Escrig, E. Bandiello, M. Scheepers, E. Edri, H. J. Bolink, *APL Mater.* **2014**, *2*, 081504.
[38] C. Momblona, L. Gil-Escrig, E. Bandiello, E. M. Hutter, M. Sessolo, K. Lederer, J. Blochwitz-Nimoth, H. J. Bolink, *Energy Environ. Sci.* **2016**, *9*, 3456.
[39] L. Gil-Escrig, C. Momblona, M.-G. La-Placa, P. P. Boix, M. Sessolo, H. J. Bolink, *Adv. Energy Mater.* **2018**, *8*, 1703506.
[40] J. B. Patel, J. Wong-Leung, S. Van Reenen, N. Sakai, J. T. W. Wang, E. S. Parrott, M. Liu, H. J. Snaith, L. M. Herz, M. B. Johnston, *Adv. Electron. Mater.* **2017**, *3*, 1600470.
[41] J. B. Patel, R. L. Milot, A. D. Wright, L. M. Herz, M. B. Johnston, *J. Phys. Chem. Lett.* **2016**, *7*, 96.
[42] A. M. Igual-Muñoz, J. Ávila, P. P. Boix, H. J. Bolink, *Sol. RRL* **2019**, 1900283, https://doi.org/10.1002/solr.201900283.
[43] E. S. Parrott, J. B. Patel, A.-A. Haghighirad, H. J. Snaith, M. B. Johnston, L. M. Herz, *Nanoscale* **2019**, *11*, 14276.
[44] J. Borchert, I. Levchuk, L. C. Snoek, M. U. Rothmann, R. Haver, H. J. Snaith, C. J. Brabec, L. M. Herz, M. B. Johnston, *ACS Appl. Mater. Interfaces* **2019**, *11*, 28851.
[45] C. L. Davies, M. R. Filip, J. B. Patel, T. W. Crothers, C. Verdi, A. D. Wright, R. L. Milot, F. Giustino, M. B. Johnston, L. M. Herz, *Nat. Commun.* **2018**, *9*, 293.
[46] P. Zhu, C. Chen, S. Gu, R. Lin, J. Zhu, *Sol. RRL* **2018**, *2*, 1700224.
[47] M. Kranjčec, I. P. Studenyak, M. V. Kurik, *J. Non-Cryst. Solids* **2009**, *355*, 54.
[48] G. D. Cody, *J. Non-Cryst. Solids* **1992**, *141*, 3.
[49] V. S. Chirvony, K. S. Sekerbayev, D. Pérez-del-Rey, J. P. Martínez-Pastor, F. Palazon, P. P. Boix, T. I. Taurbayev, M. Sessolo, H. J. Bolink, *J. Phys. Chem. Lett.* **2019**, *10*, 5167.
[50] A. Armin, M. Velusamy, P. Wolfer, Y. Zhang, P. L. Burn, P. Meredith, A. Pivrikas, *ACS Photonics* **2014**, *1*, 173.
[51] J. B. Patel, Q. Lin, O. Zadvorna, C. L. Davies, L. M. Herz, M. B. Johnston, *J. Phys. Chem. Lett.* **2018**, *9*, 263.
[52] Q. Lin, A. Armin, P. L. Burn, P. Meredith, *Nat. Photonics* **2015**, *9*, 687.
[53] M. B. Johnston, *Nat. Photonics* **2015**, *9*, 634.
[54] T. W. Crothers, R. L. Milot, J. B. Patel, E. S. Parrott, J. Schlipf, P. Müller-Buschbaum, M. B. Johnston, L. M. Herz, *Nano Lett.* **2017**, *17*, 5782.
[55] Q. Lin, A. Armin, R. C. R. Nagiri, P. L. Burn, P. Meredith, *Nat. Photonics* **2015**, *9*, 106.
[56] J. Nelson, *The Physics of Solar Cells*, Imperial College Press, London, UK **2003**.
[57] J. Wang, W. Fu, S. Jariwala, I. Sinha, A. K.-Y. Jen, D. S. Ginger, *ACS Energy Lett.* **2019**, *4*, 222.
[58] E. Yablonovitch, T. Tiedje, H. Witzke, *Appl. Phys. Lett.* **1982**, *41*, 953.
[59] L. M. Pazos-Outón, T. P. Xiao, E. Yablonovitch, *J. Phys. Chem. Lett.* **2018**, *9*, 1703.
[60] R. Brendel, H. J. Queisser, *Sol. Energy Mater. Sol. Cells* **1993**, *29*, 397.
[61] S. D. Stranks, G. E. Eperon, G. Grancini, C. Menelaou, M. J. P. Alcocer, T. Leijtens, L. M. Herz, A. Petrozza, H. J. Snaith, *Science* **2013**, *342*, 341.
[62] H. J. Snaith, L. Schmidt-Mende, M. Grätzel, M. Chiesa, *Phys. Rev. B* **2006**, *74*, 045306.
[63] T. Kirchartz, F. Staub, U. Rau, *ACS Energy Lett.* **2016**, *1*, 731.
[64] T. Kirchartz, U. Rau, *Adv. Energy Mater.* **2018**, *8*, 1703385.
[65] T. Kirchartz, L. Krückemeier, E. L. Unger, *APL Mater.* **2018**, *6*, 100702.